

Cite this: *Chem. Sci.*, 2021, 12, 5818

All publication charges for this article have been paid for by the Royal Society of Chemistry

Received 21st January 2021  
Accepted 11th March 2021

DOI: 10.1039/d1sc00392e

rsc.li/chemical-science

## Proton-conductive coordination polymer glass for solid-state anhydrous proton batteries†

Nattapol Ma,<sup>a</sup> Soracha Kosasang,<sup>b</sup> Atsushi Yoshida<sup>a</sup> and Satoshi Horike<sup>a,c,d,e</sup>

Designing solid-state electrolytes for proton batteries at moderate temperatures is challenging as most solid-state proton conductors suffer from poor moldability and thermal stability. Crystal–glass transformation of coordination polymers (CPs) and metal–organic frameworks (MOFs) *via* melt-quenching offers diverse accessibility to unique properties as well as processing abilities. Here, we synthesized a glassy-state CP, [Zn<sub>3</sub>(H<sub>2</sub>PO<sub>4</sub>)<sub>6</sub>(H<sub>2</sub>O)<sub>3</sub>](1,2,3-benzotriazole), that exhibited a low melting temperature (114 °C) and a high anhydrous single-ion proton conductivity (8.0 × 10<sup>−3</sup> S cm<sup>−1</sup> at 120 °C). Converting crystalline CPs to their glassy-state counterparts *via* melt-quenching not only initiated an isotropic disordered domain that enhanced H<sup>+</sup> dynamics, but also generated an immersive interface that was beneficial for solid electrolyte applications. Finally, we demonstrated the first example of a rechargeable all-solid-state H<sup>+</sup> battery utilizing the new glassy-state CP, which exhibited a wide operating-temperature range of 25 to 110 °C.

### Introduction

The proton (H<sup>+</sup>) has a diameter of 0.84 fm and is easily localized in the solid state.<sup>1</sup> Fast-moving protons in solids are difficult to achieve, whereas solid-state H<sup>+</sup> conductors are widely used in various electrochemical applications, including fuel cells, electrochemical catalysis, and sensors.<sup>2</sup> Proton batteries are a new class of secondary batteries employing protons instead of metal ions as charge carriers.<sup>3,4</sup> They consist of faradaic electrodes and acidic electrolytes. Since the H<sup>+</sup> charge radius is significantly smaller than that of other ions, faster ion migration and negligible volume changes upon H<sup>+</sup> insertion/desertion are expected. Additionally, replacing high-cost Li<sup>+</sup> with cheaper and

more abundant H<sup>+</sup> provides a promising platform for environmentally benign and intrinsically safe energy storage.<sup>5–7</sup> Redox-active organic molecules, such as quinone-functionalized conductive polymers,<sup>4,8</sup> and metal oxides, including MoO<sub>3</sub>, WO<sub>3</sub>, and H<sub>x</sub>IrO<sub>4</sub>, are available as H<sup>+</sup> electrodes.<sup>9–11</sup> Though proton batteries show a smaller specific capacity with a limited number of applications, as compared to their metallic counterparts, diffusion-free charge transport *via* the Grotthuss mechanism in a defective, Prussian blue analog establishes a high-rate capability (380 A g<sup>−1</sup>) and extends cycling stability to over 0.5 million charge–discharge cycles, which is a unique advantage of aqueous proton batteries.<sup>6,12,13</sup> In spite of various choices of electrodes, electrolytes are mostly limited to aqueous H<sub>2</sub>SO<sub>4</sub> or H<sub>3</sub>PO<sub>4</sub>, which dictates the operating-temperature window and selection of usable electrodes.<sup>8,13–15</sup>

Safely extending the operating-temperature window to ~100 °C is essential for H<sup>+</sup> batteries to tolerate internal/external heat generation so that they can be used in various high-temperature applications, such as rescue/inspection robots, space exploration, and measure-while-drilling (MWD) equipment in the oil and gas industries.<sup>16</sup> As employing a conventional aqueous electrolyte is not possible at these high temperatures, solid-state H<sup>+</sup> batteries with anhydrous solid electrolytes would be more suitable. There are no reports of solid-state H<sup>+</sup> batteries working near or above 100 °C due to the difficulties in achieving high anhydrous H<sup>+</sup> conductivity, high-temperature stability, and moldability required for H<sup>+</sup> conductors.<sup>17</sup> Apart from achieving a high H<sup>+</sup> conductivity value (near 10<sup>−2</sup> S cm<sup>−1</sup>), high thermal/chemical stability, processing ability, and ion selectivity are also needed to expand the practicality of solid-state electrolytes. Single-ion conductivity in

<sup>a</sup>Department of Synthetic Chemistry and Biological Chemistry, Graduate School of Engineering, Kyoto University, Katsura, Nishikyo-ku, Kyoto 615-8510, Japan. E-mail: horike@icems.kyoto-u.ac.jp

<sup>b</sup>Department of Chemical and Biomolecular Engineering, School of Energy Science and Engineering, Vidyasirimedhi Institute of Science and Technology, Rayong, 21210, Thailand

<sup>c</sup>AIST-Kyoto University Chemical Energy Materials Open Innovation Laboratory (ChEM-OIL), National Institute of Advanced Industrial Science and Technology (AIST), Yoshida-Honmachi, Sakyo-ku, Kyoto 606-8501, Japan

<sup>d</sup>Institute for Integrated Cell-Material Sciences, Institute for Advanced Study, Kyoto University, Yoshida-Honmachi, Sakyo-ku, Kyoto 606-8501, Japan

<sup>e</sup>Department of Materials Science and Engineering, School of Molecular Science and Engineering, Vidyasirimedhi Institute of Science and Technology, Rayong, 21210, Thailand

† Electronic supplementary information (ESI) available: Experimental details, PXRD, solid PXRD, <sup>31</sup>P MAS NMR, TG, and FTIR results, Nyquist plots, long-term conductivity measurements, transport number measurements, cross-sectional SEM images, and a solid state H<sup>+</sup> battery. CCDC 2044808. For ESI and crystallographic data in CIF or other electronic format see DOI: 10.1039/d1sc00392e



solid-state electrolytes is a core factor that promotes charge-transport efficiency and prevents anion polarization.<sup>18,19</sup> Discontinuities along the electrode–electrolyte interfaces and grain boundaries are primary bottlenecks for efficient utilization of solid electrolytes.<sup>17,20,21</sup> H<sup>+</sup> conductivity at the grain boundary of most crystalline compounds requires a higher migration activation energy than that required by H<sup>+</sup> conductivity through the bulk crystal (grain boundaries contribute up to 40–50% of the overall resistance for Li<sup>+</sup> conductors).<sup>22–25</sup>

Coordination polymers (CPs) and metal–organic frameworks (MOFs) exhibiting high H<sup>+</sup> conductivity over a wide temperature regime (~200 °C) represent a new class of solid-state H<sup>+</sup> conductors.<sup>26–29</sup> Despite their remarkable H<sup>+</sup> conductivity, their crystalline nature hinders their processing ability, thus limiting their practicality.<sup>30</sup> The glassy state of CP/MOFs is a strong platform to tackle these issues, and there have been increasing numbers of glassy-state CPs recently made from crystalline-state CPs.<sup>31–34</sup> Some of these glassy-state CPs show anhydrous H<sup>+</sup> conductivity superior to that of their crystalline counterparts by several orders of magnitude.<sup>35,36</sup> Moreover, the vitrifying/melting behavior provides these CPs with processing capabilities and forms a grain-boundary free monolith and a flawless heterogeneous interface.<sup>31–34,37–41</sup>

To address this issue, we have developed a new H<sup>+</sup>-conductive CP glass suitable for high-temperature anhydrous solid-state H<sup>+</sup> batteries. By optimizing the pK<sub>a</sub> value of the component with 1,2,3-benzotriazole (BTA, pK<sub>a</sub> 1.6) and the extended hydrogen-bonding network in Zn<sup>2+</sup>-based CPs, the material demonstrated high anhydrous H<sup>+</sup> conductivity (8.0 × 10<sup>−3</sup> S cm<sup>−1</sup> at 120 °C), relatively low melting point (114 °C), and mechanical softness (42.8 Pa s at 120 °C), which are suitable for electrolytes. The structure and properties were characterized by single-crystal X-ray diffraction (SC-XRD), thermal gravimetric analysis (TGA), differential scanning calorimetry (DSC), dynamic mechanical analysis (DMA), impedance spectroscopy, electromotive force measurements, and solid-state NMR. We also demonstrated a full-cell evaluation of the anhydrous solid-state H<sup>+</sup> batteries at 25, 100, and 110 °C.

## Results and discussion

### Crystal structure of [Zn<sub>3</sub>(H<sub>2</sub>PO<sub>4</sub>)<sub>6</sub>(H<sub>2</sub>O)<sub>3</sub>](BTA) (**1a**)

Zinc oxide, phosphoric acid, and BTA were subjected to mechanical milling to form the CP (**1a**) as a white crystalline powder. SC-XRD analysis of **1a** provided its chemical formula, [Zn<sub>3</sub>(H<sub>2</sub>PO<sub>4</sub>)<sub>6</sub>(H<sub>2</sub>O)<sub>3</sub>](BTA), and it was found to exist as a one-dimensional (1D) chain along the *a*-axis (Fig. 1). Three crystallographically independent octahedral Zn<sup>2+</sup> ions were identified, each with six bridging H<sub>2</sub>PO<sub>4</sub><sup>−</sup> anions and one water molecule coordinated to them (Fig. 1A). BTA was stacked in a 1D fashion along the *a*-axis and surrounded by six chains of ZnO<sub>6</sub> octahedra, which orderly arranged in the *bc* plane due to hydrogen-bonding interactions (Fig. 1B and C). Furthermore, **1a** is an isostructure of previously reported [Zn<sub>3</sub>(H<sub>2</sub>PO<sub>4</sub>)<sub>6</sub>(H<sub>2</sub>O)<sub>3</sub>](benzimidazole),<sup>38</sup> and it is expected that the dynamics of the phosphates bridging the Zn<sup>2+</sup> ions (through a single

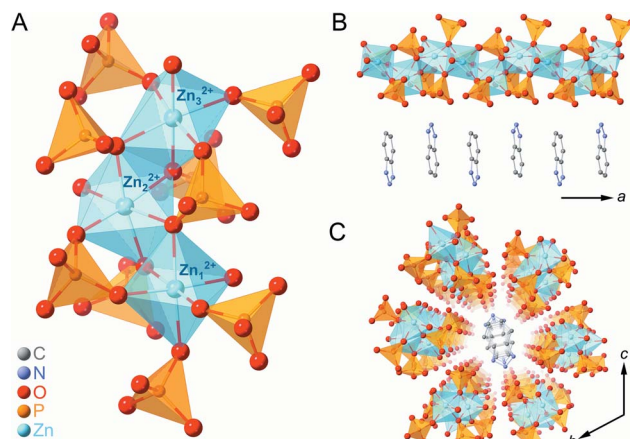


Fig. 1 (A) Local coordination geometry in **1a**. (B) Crystal structure of the one-dimensional (1D) chain along the *a*-axis. (C) Packing structure of **1a** on the *bc*-plane. Zn, P, O, C, and N atoms are represented by light blue, orange, red, grey, and blue spheres, respectively. H atoms are omitted for clarity.

bridging oxygen atom ( $\mu_2$ ) and the non-coordinating BTA could facilitate an anhydrous H<sup>+</sup> migration.<sup>2,38,42,43</sup>

The gram-scale synthesis of **1a** was feasible *via* mechanical milling for 1 h followed by vacuum drying for 3.5 h to remove excess water molecules. Powder X-ray diffraction (PXRD) of **1a** (Fig. S1<sup>†</sup>) demonstrated a pattern identical to the simulated SC-XRD pattern. The absence of residual free phosphoric acid in **1a** was confirmed using both inductively coupled plasma emission spectroscopy (ICP-ES) and <sup>31</sup>P magic-angle spinning (MAS) solid-state NMR (Fig. S2<sup>†</sup>).<sup>44</sup> A P to Zn ratio (1 : 1.97) slightly lower than the theoretical ratio (1 : 2) suggested the presence of a small amount of structural defects. All peaks in <sup>31</sup>P NMR were located in the range of orthophosphate, suggesting that no condensation occurs during the mechanical synthesis.<sup>45–47</sup> TGA of **1a** showed a gradual weight loss due to the release of coordinated water at 100 °C (Fig. S4<sup>†</sup>). The total weight loss of dehydrated **1a** is equivalent to the release of three coordinated water molecules (5.7 wt%). This dehydrated state is henceforth denoted as **1**. A reversible structural change between **1a** and **1** upon water adsorption and desorption was observed by PXRD (Fig. S5<sup>†</sup>).<sup>48–50</sup> The release of each water molecule from the octahedral (*O<sub>h</sub>*) coordination sphere caused the 1D chain structure to deform around the Zn<sup>2+</sup> ion. Under ambient air, **1** converted to **1a** by capturing atmospheric moisture.<sup>38</sup>

### Crystal melting and glass formation

Differential thermal analysis of **1a** by TGA (Fig. S4<sup>†</sup>) showed two endothermic peaks due to the release of coordinated water and crystal-to-liquid transformation and only the latter peak was observed in **1**. DSC of **1** (Fig. 2A) showed an endothermic peak with an onset melting point (*T<sub>m</sub>*) of 114 °C. Two minor endothermic peaks before that of the *T<sub>m</sub>* were assigned to the dehydration of adsorbed water during the measurement setup.<sup>33</sup> The *T<sub>m</sub>* of **1** was 50 °C lower than that of the isostructure, [Zn<sub>3</sub>(H<sub>2</sub>PO<sub>4</sub>)<sub>6</sub>(H<sub>2</sub>O)<sub>3</sub>](benzimidazole), as BTA exhibits



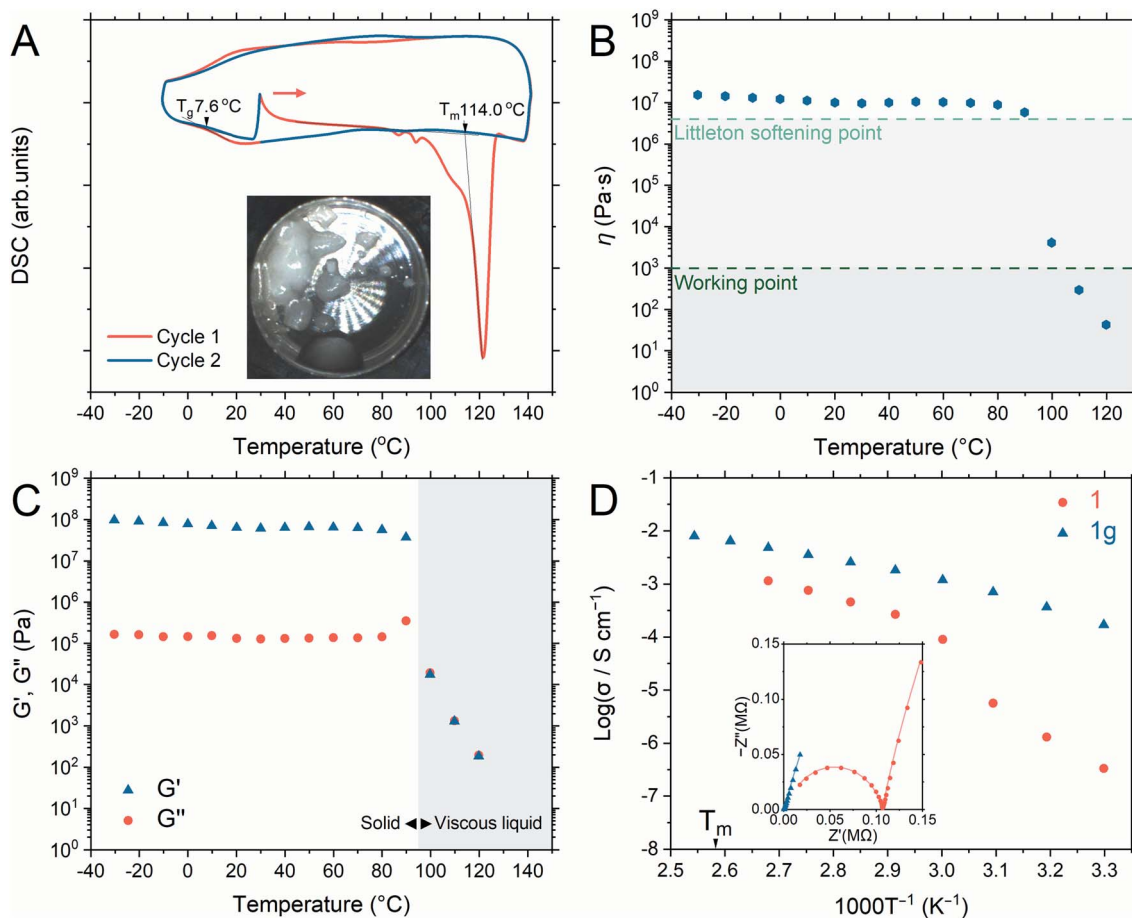


Fig. 2 (A) First- (blue) and second-cycle (red) DSC profiles of **1** from  $-10$  to  $140$  °C (begin with a heating step from  $30$  °C). The inset shows a photo of **1m** at  $140$  °C. (B) Temperature-dependent viscosity of **1g**. (C) DMA of **1g** from  $-30$  to  $120$  °C (heating rate of  $2$  °C  $\text{min}^{-1}$ ). The storage ( $G'$ ) and loss ( $G''$ ) moduli were marked as ( $\blacktriangle$ ) and ( $\bullet$ ), respectively. (D) Arrhenius plots of the anhydrous conductivity of **1** ( $\bullet$ ) and **1g** ( $\blacktriangle$ ) under an Ar atmosphere. The inset shows the Nyquist plot of **1** ( $\bullet$ ) and **1g** ( $\blacktriangle$ ) at  $50$  °C.

lower  $T_m$  and  $pK_a$  values than those of benzimidazole.<sup>31,33</sup> Additionally, no significant weight loss was seen at  $120$  °C after 12 h, confirming a stable liquid state (Fig. S6†). The liquid/molten state of **1** is henceforth referred to as **1m**. The first cooling process in DSC confirmed the vitrification of **1m** to a glassy state of **1** (denoted as **1g**) that demonstrated a glass transition temperature ( $T_g$ ) of  $7.6$  °C, exhibiting no Bragg diffraction, and was categorized as melt-quenched glass (MGQ) (Fig. S7†).<sup>34</sup>

DMA and viscosity evaluation of **1g** further determined its processing ability, where its viscosity (Fig. 2B) was observed above the Littleton softening point ( $10^{6.6}$  Pa s) from  $-30$  to  $90$  °C until it sharply decreased below the working point regime ( $10^3$  Pa s) above  $100$  °C. The working point defines the viscosity regime in which the viscosity of a substance is equivalent to that of soda-lime-silica glass above  $1100$  °C (suitable for industrial forming processes).<sup>51</sup> The storage modulus ( $G'$ ) dominated the loss modulus ( $G''$ ) from  $-30$  to  $90$  °C, verifying the solid character of **1g** (Fig. 2C). Immediate reduction of  $G'$  at  $100$  °C represents the softening of **1g**, and the  $G'/G''$  crossover indicates the range in which **1g** starts to behave like a viscous liquid.<sup>31,52</sup>

### Anhydrous $H^+$ conductivity

We measured the  $H^+$  conductivity of **1** and **1g** via variable-temperature alternating current (AC) impedance under an Ar atmosphere to exclude the influence of water molecules (Fig. 2D and S9†). The Nyquist plots were fitted with a single impedance response corresponding to the bulk resistance without the grain-boundary region.<sup>52,53</sup> The conductivity of **1** was measured from  $30$  to  $100$  °C, where the crystalline phase of **1** was preserved. We observed conductivity values of  $3.3 \times 10^{-7}$  S  $\text{cm}^{-1}$  and  $9.0 \times 10^{-5}$  S  $\text{cm}^{-1}$  at  $30$  and  $60$  °C, respectively. The conductivity value increased rapidly upon heating, reaching  $1.2 \times 10^{-3}$  S  $\text{cm}^{-1}$  at  $100$  °C. The activation energy of **1** from  $30$  to  $60$  °C was  $1.22$  eV. Above  $60$  °C, the Arrhenius plot flattened and the activation energy reduced to  $0.57$  eV. Utilizing BTA with its low  $pK_a$  in **1** provided higher conductivity values than those of the isostructure  $[\text{Zn}_3(\text{H}_2\text{PO}_4)_6](\text{HBim})$  at  $30$  °C ( $1.2 \times 10^{-7}$  S  $\text{cm}^{-1}$ ) and  $60$  °C ( $1.5 \times 10^{-5}$  S  $\text{cm}^{-1}$ ).<sup>38</sup>

To highlight the advantage of glass transformation on ionic conductivity, we prepared a monolith (**1g**) via melt-quenching directly into the electrochemical cell for impedance analysis. Upon the crystalline-to-glassy state transformation, only the



bulk impedance response pattern was obtained (Fig. S9†) and it was identical to that of **1a** in the higher temperature range. The Arrhenius plot (Fig. 2D) shows two different activation energy regimes: 0.59 eV between 30 and 60 °C and 0.39 eV from 60 to 120 °C. At 30 °C, **1g** exhibited a conductivity value of  $3.3 \times 10^{-4} \text{ S cm}^{-1}$ , which increased to  $4.9 \times 10^{-3} \text{ S cm}^{-1}$  and  $6.5 \times 10^{-3} \text{ S cm}^{-1}$  at 100 and 110 °C, respectively. A conductivity value of  $8.0 \times 10^{-3}$  was achieved at 120 °C (molten state, **1m**). Long-term conductivity retention was also evaluated. After 12 h, less than 4% and 10% loss in conductivity was observed at 100 and 120 °C, respectively (Fig. S10†). The contribution of the ions of interest to the total current can be distinguished *via* the  $\text{H}^+$  transport number (transference number) measurements.<sup>52,54</sup> The transport numbers of most aqueous and ionic liquid electrolytes are lower than 0.6.<sup>54–56</sup> The transport number of **1m** was elucidated *via* electromotive force (EMF) measurements, which were conducted for different hydrogen partial pressure ( $-\ln(P_1/P_2)$ ) values of 0.22, 0.51, 0.69, 0.92, and 1.61) at 120 °C (Fig. S11†).<sup>57</sup> According to eqn S1 (ESI),† the  $\text{H}^+$  transference number of **1g** is 1.0, indicating an ideal single-ion  $\text{H}^+$  conductivity. The absence of anion mobility suggests that the coordination networks are retained even in the molten state.<sup>31,58</sup>

### Proton dynamics in **1** and **1g**

The  $\text{H}^+$  conductivity would be dominated by either the phosphate or BTA dynamics; therefore, we utilized variable-temperature  $^1\text{H}$  MAS solid-state NMR to study their mobilities (Fig. 3). The peaks from 8.1–8.5 and 5.8–6.1 ppm were assigned to the phosphate and BTA  $\text{H}^+$ , respectively.<sup>44,52</sup> The substantial narrowing and intensifying of the peaks between 50 and 75 °C suggested a significant increase in both the phosphate and BTA dynamics. The molecular motion of BTA initiates at the temperature above 50 °C as the BTA peaks are barely distinguishable at 25 and 50 °C (Fig. 3A).<sup>38</sup> The  $\text{H}^+$  mobilities of **1g** and **1** were compared at 25 and 50 °C as well as at 50 and 75 °C,

where the narrower and more intense peaks of **1g** demonstrated its higher  $\text{H}^+$  mobility than that of **1** (Fig. 3B). This higher degree of  $\text{H}^+$  mobility was promoted by a disordered structure formed in **1g**. Furthermore, the BTA dynamics were observable in **1g** even at temperatures lower than 60 °C, which agrees with the impedance response and lower activation energy of **1g**. Additionally, hydrogen-bond formations are indicated by downfield shifts.<sup>59</sup>

### Electrode–electrolyte interface

Discontinuities along the heterogeneous interface inhibit practical applications of solid-state electrolytes.<sup>17</sup> Therefore, we are interested in the  $\text{H}^+$ -conductivity integration and moldability of **1g** as a grain boundary-free immersive solid electrolyte (Fig. 4A). Additionally, the lower  $T_m$  of **1** would prevent the anode/cathode materials from degrading during the fabrication process.<sup>8,9,12,13</sup> A carbon fiber (CF) electrode was pressed to **1m** at 120 °C and quenched to room temperature to provide the electrode–electrolyte interface (CF–**1g**). Cross-sectional scanning electron microscopy (SEM) images of CF–**1g** were collected (Fig. 4B, S12A, and B†), where neither a distinguishable solid–electrolyte interface nor grain boundaries were observed.<sup>60</sup> Optimum contact between the CF layer and **1g** domain was achieved as **1m** can penetrate the CF, generating a fully immersed environment. Fig. 4C shows a cross-sectional SEM reference image of the pristine CF. Energy-dispersive X-ray (EDX) mapping (Fig. 4D–G) further elucidated the position of the CF electrode (intense C) with homogeneously distributed Zn, P, and O signals. To amplify the benefits of melt-quenching glass, we re-examined the morphological alteration of CF–**1g** after recrystallization. **1g** undergoes the recrystallization process upon humidity exposure and transforms back to **1a**. As confirmed by PXRD (Fig. S13†), atmospheric humidity (65% relative humidity) at room temperature (25 °C) is sufficient for the recrystallization to occur within 4 h. Fig. S12C and D† revealed grain boundaries and fractures formed throughout the recrystallized **1g** matrix, especially in the region where the CF and **1g** co-exist.

### Solid-state $\text{H}^+$ battery under anhydrous conditions

Adequately high  $\text{H}^+$  conductivity, single-ion conductivity, low processing temperatures, and thermal/electrochemical stabilities motivated us to apply **1g** as a solid electrolyte for  $\text{H}^+$  batteries.  $\text{MoO}_3$  and  $\text{Cu}^{\text{II}}[\text{Fe}^{\text{III}}(\text{CN})_6]_{2/3} \cdot 4\text{H}_2\text{O}$  (CuFe-TBA) were selected as a model cathode and anode, respectively.<sup>10,12</sup> As a reference, we also evaluated a full-cell configuration in 2 M  $\text{H}_2\text{SO}_4$  solution at 25 °C. It exhibited a discharge capacity of  $35.8 \text{ mA h g}^{-1}$  at  $100 \text{ mA g}^{-1}$  (Fig. S14†). The specific capacity was calculated based on the cathode mass. The distance between the electrodes was *ca.* 1 cm.<sup>12</sup> The solid-state  $\text{H}^+$  battery was prepared by immersing both electrodes (1 cm separations) in **1m** at 120 °C under an Ar atmosphere, where subsequent quenching to room temperature gave the **1g** electrolyte. Fig. 4H and S15A† show the charge–discharge profiles (from 0 to 1.2 V) and rate performance evaluation of solid-state  $\text{H}^+$  batteries under an Ar atmosphere utilizing the **1g** electrolyte at 25 °C. The

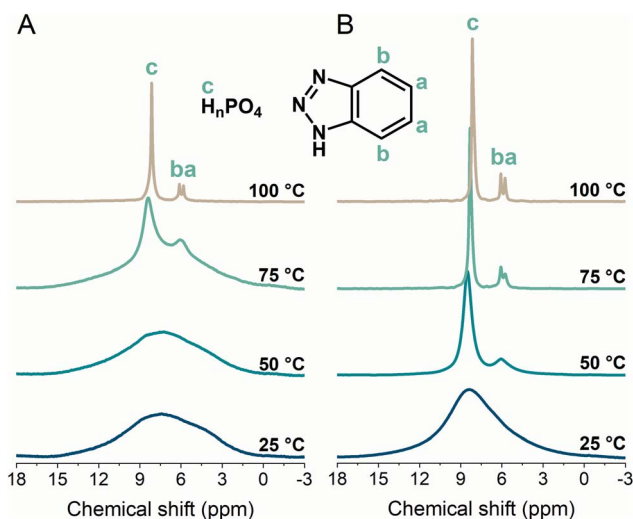


Fig. 3 Variable-temperature  $^1\text{H}$  magic-angle spinning (MAS) solid-state NMR spectra (MAS 8 kHz) of (A) **1** and (B) **1g** from 25 to 100 °C.



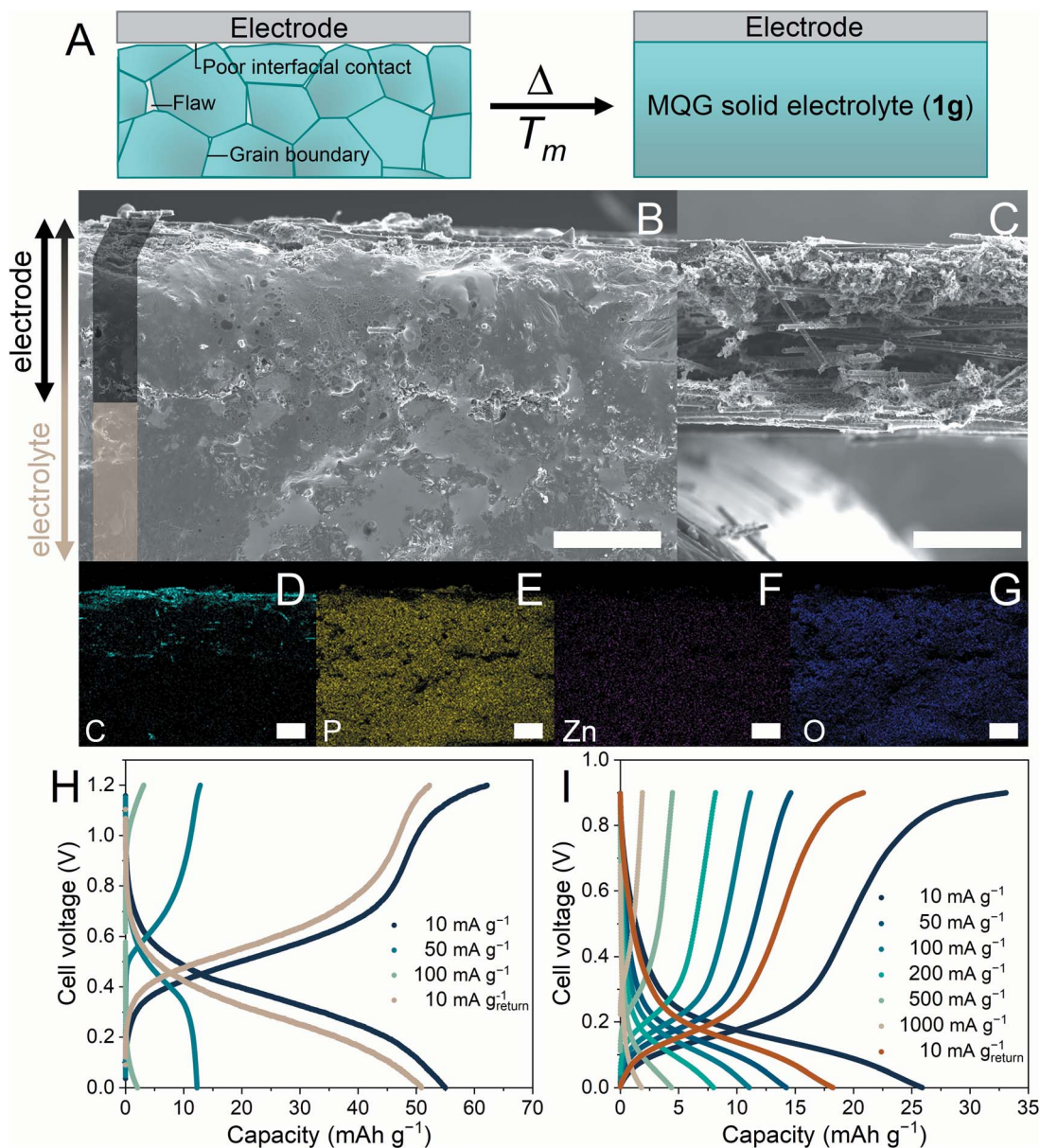


Fig. 4 (A) Schematic representation of the interfaces/flaws within the polycrystalline solid electrolyte (left) and MQG solid electrolyte proposed in this work (**1g**). Cross-sectional scanning electron microscopy (SEM) images ( $\times 150$  magnification) of (B) the electrode–solid-state electrolyte interface (CF–**1g**) and (C) CF electrode. Scale bar = 150  $\mu\text{m}$ . Energy-dispersive X-ray (EDX) mapping for (D) C, (E) P, (F) Zn, and (G) O. Scale bar = 100  $\mu\text{m}$ . Full-cell charge–discharge profiles utilizing **1g** as a solid-state electrolyte at (H) 25  $^\circ\text{C}$  and (I) 100  $^\circ\text{C}$ .

highest discharge capacity was 55.4  $\text{mA h g}^{-1}$  at 10  $\text{mA g}^{-1}$ . Another advantage the **1g**-electrolyte system has over the aqueous system is its large operating-temperature range. The elevated-temperature  $\text{H}^+$  battery was evaluated at 100 and 110  $^\circ\text{C}$  under an Ar atmosphere (Fig. 4I and S15C†) and the redox potentials of both electrodes reduced, corresponding to the change in free energy.<sup>61,62</sup> As shown in Fig. S15B and D,† rate performances improved significantly as the ionic conductivity of **1g** was enhanced.<sup>2</sup> In a high-temperature regime, electrodes would show an excessive self-discharge as well as a thermal structural distortion limiting the protonation/deprotonation processes, causing a net loss of capacity. For instance, in a Li-ion battery, capacity fading was observed in  $\text{Li}_3\text{V}_2(\text{PO}_4)_3$  as

elevated temperature promotes a larger structural distortion between  $\text{Li}_3\text{V}_2(\text{PO}_4)_3$  and  $\text{V}_2(\text{PO}_4)_3$  limiting the re-insertion of  $\text{Li}^+$ .<sup>63</sup> Additionally, 76% of the original capacity was retained after 1000 cycles of the charge–discharge process at 110  $^\circ\text{C}$  (Fig. S16†). We also attempted to demonstrate a solid-state  $\text{H}^+$  battery using crystalline **1** with a similar configuration and an identical anode and cathode. However, charging and discharging processes were not possible at 25  $^\circ\text{C}$  nor under low-current (10  $\text{mA g}^{-1}$ ) conditions, even though the thickness of this electrolyte was ten times smaller than that of the **1g** electrolyte. This emphasizes the importance of interface engineering that endows soft glass materials with high  $\text{H}^+$  conductivity and moldability.<sup>17,20,21</sup>



## Conclusions

We synthesized a new H<sup>+</sup> conductive CP, [Zn<sub>3</sub>(H<sub>2</sub>PO<sub>4</sub>)<sub>6</sub>(-H<sub>2</sub>O)<sub>3</sub>](BTA), where the dehydrated state (**1**) integrated promising anhydrous H<sup>+</sup> conductivity (1.2 × 10<sup>-3</sup> S cm<sup>-1</sup> at 100 °C) and relatively low melting point (114 °C). The melt-quenched glass of **1** (**1g**) enhanced the H<sup>+</sup> dynamics of both phosphate and BTA, resulting in a H<sup>+</sup> conductivity value of 8.0 × 10<sup>-3</sup> S cm<sup>-1</sup>, a H<sup>+</sup> transference number of 1.0, and a viscosity of 42.8 Pa s at 120 °C. The coexistence of high conductivity, transport number, and moldability of **1g**, as well as its flawless interface, encouraged us to implement it in solid-state H<sup>+</sup> battery applications. A solid-state H<sup>+</sup> battery with an operating temperature range above room temperature (25–110 °C) was demonstrated for the first time. The tuning capability of the CP glass H<sup>+</sup> conductivity, working temperature, and softness could provide H<sup>+</sup> batteries with wider applications.

## Author contributions

S. H. designed the project, and N. M. and A. Y. synthesized the compounds. S. K. collected and analyzed solid-state NMR measurements. N. M. collected and analyzed SC-XRD, PXRD, TGA, SEM, DSC, ICP-ES, DMA, FTIR, conductivity and transport number measurements and battery evaluation. S. H. and N. M. wrote the paper.

## Conflicts of interest

There are no conflicts to declare.

## Acknowledgements

The work was supported by the Japan Society for the Promotion of Science (JSPS) for a Grant-in-Aid for Scientific Research (B) (JP18H02032), Challenging Research (Exploratory) (JP19K22200) from the Ministry of Education, Culture, Sports, Science and Technology, Japan, and the Adaptable and Seamless Technology Transfer Program through Target-driven R&D (A-STEP) from the Japan Science and Technology, Japan. N. M. acknowledges the Japanese Government (MEXT) scholarship.

## References

- R. Pohl, A. Antognini, F. Nez, F. D. Amaro, F. Biraben, J. M. R. Cardoso, D. S. Covita, A. Dax, S. Dhawan, L. M. P. Fernandes, A. Giesen, T. Graf, T. W. Hänsch, P. Indelicato, L. Julien, C.-Y. Kao, P. Knowles, E.-O. Le Bigot, Y.-W. Liu, J. A. M. Lopes, L. Ludhova, C. M. B. Monteiro, F. Mulhauser, T. Nebel, P. Rabinowitz, J. M. F. dos Santos, L. A. Schaller, K. Schuhmann, C. Schwob, D. Taqqu, J. F. C. A. Veloso and F. Kottmann, *Nature*, 2010, **466**, 213–216.
- K.-D. Kreuer, *Chem. Mater.*, 1996, **8**, 610–641.
- K. Nueangnoraj, T. Tomai, H. Nishihara, T. Kyotani and C.-J. Cai, *Carbon*, 2016, **107**, 831–836.
- R. Emanuelsson, M. Sterby, M. Strømme and M. Sjödin, *J. Am. Chem. Soc.*, 2017, **139**, 4828–4834.
- M. Armand and J. M. Tarascon, *Nature*, 2008, **451**, 652–657.
- X. Ji, *Energy Environ. Sci.*, 2019, **12**, 3203–3224.
- G. Liang, F. Mo, X. Ji and C. Zhi, *Nat. Rev. Mater.*, 2021, **6**, 109–123.
- C. Strietzel, M. Sterby, H. Huang, M. Strømme, R. Emanuelsson and M. Sjödin, *Angew. Chem., Int. Ed.*, 2020, **59**, 9631–9638.
- H. Jiang, J. J. Hong, X. Wu, T. W. Surta, Y. Qi, S. Dong, Z. Li, D. P. Leonard, J. J. Holoubek, J. C. Wong, J. J. Razink, X. Zhang and X. Ji, *J. Am. Chem. Soc.*, 2018, **140**, 11556–11559.
- X. Wang, Y. Xie, K. Tang, C. Wang and C. Yan, *Angew. Chem., Int. Ed.*, 2018, **57**, 11569–11573.
- P. Lemaire, O. Sel, D. Alves Dalla Corte, A. Iadecola, H. Perrot and J.-M. Tarascon, *ACS Appl. Mater. Interfaces*, 2020, **12**, 4510–4519.
- X. Wu, J. J. Hong, W. Shin, L. Ma, T. Liu, X. Bi, Y. Yuan, Y. Qi, T. W. Surta, W. Huang, J. Neuefeind, T. Wu, P. A. Greaney, J. Lu and X. Ji, *Nat. Energy*, 2019, **4**, 123–130.
- X. Wu, S. Qiu, Y. Xu, L. Ma, X. Bi, Y. Yuan, T. Wu, R. Shahbazian-Yassar, J. Lu and X. Ji, *ACS Appl. Mater. Interfaces*, 2020, **12**, 9201–9208.
- L. Yan, J. Huang, Z. Guo, X. Dong, Z. Wang and Y. Wang, *ACS Energy Lett.*, 2020, **5**, 685–691.
- H. Jiang, W. Shin, L. Ma, J. J. Hong, Z. Wei, Y. Liu, S. Zhang, X. Wu, Y. Xu, Q. Guo, M. A. Subramanian, W. F. Stickle, T. Wu, J. Lu and X. Ji, *Adv. Energy Mater.*, 2020, **10**, 2000968.
- X. Lin, M. Salari, L. M. R. Arava, P. M. Ajayan and M. W. Grinstaff, *Chem. Soc. Rev.*, 2016, **45**, 5848–5887.
- Q. Zhao, S. Stalin, C.-Z. Zhao and L. A. Archer, *Nat. Rev. Mater.*, 2020, **5**, 229–252.
- J. Evans, C. A. Vincent and P. G. Bruce, *Polymer*, 1987, **28**, 2324–2328.
- S. S. Park, Y. Tulchinsky and M. Dincă, *J. Am. Chem. Soc.*, 2017, **139**, 13260–13263.
- J. van den Broek, S. Afyon and J. L. M. Rupp, *Adv. Energy Mater.*, 2016, **6**, 1600736.
- X. Han, Y. Gong, K. Fu, X. He, G. T. Hitz, J. Dai, A. Pearse, B. Liu, H. Wang, G. Rubloff, Y. Mo, V. Thangadurai, E. D. Wachsman and L. Hu, *Nat. Mater.*, 2017, **16**, 572–579.
- P. G. Bruce and A. West, *J. Electrochem. Soc.*, 1983, **130**, 662.
- Y. Inaguma, C. Liqun, M. Itoh, T. Nakamura, T. Uchida, H. Ikuta and M. Wakihara, *Solid State Commun.*, 1993, **86**, 689–693.
- R. Murugan, V. Thangadurai and W. Weppner, *Angew. Chem., Int. Ed.*, 2007, **46**, 7778–7781.
- J. A. Dawson, P. Canepa, T. Famprikis, C. Masquelier and M. S. Islam, *J. Am. Chem. Soc.*, 2018, **140**, 362–368.
- S. Horike, D. Umeyama and S. Kitagawa, *Acc. Chem. Res.*, 2013, **46**, 2376–2384.
- T. Yamada, K. Otsubo, R. Makiura and H. Kitagawa, *Chem. Soc. Rev.*, 2013, **42**, 6655–6669.
- P. Ramaswamy, N. E. Wong and G. K. H. Shimizu, *Chem. Soc. Rev.*, 2014, **43**, 5913–5932.
- D.-W. Lim and H. Kitagawa, *Chem. Rev.*, 2020, **120**, 8416–8467.



- 30 T. Inada, T. Kobayashi, N. Sonoyama, A. Yamada, S. Kondo, M. Nagao and R. Kanno, *J. Power Sources*, 2009, **19**, 1085–1088.
- 31 D. Umeyama, S. Horike, M. Inukai, T. Itakura and S. Kitagawa, *J. Am. Chem. Soc.*, 2015, **137**, 864–870.
- 32 T. D. Bennett, Y. Yue, P. Li, A. Qiao, H. Tao, N. G. Greaves, T. Richards, G. I. Lampronti, S. A. T. Redfern, F. Blanc, O. K. Farha, J. T. Hupp, A. K. Cheetham and D. A. Keen, *J. Am. Chem. Soc.*, 2016, **138**, 3484–3492.
- 33 T. D. Bennett and S. Horike, *Nat. Rev. Mater.*, 2018, **3**, 431–440.
- 34 S. Horike, S. S. Nagarkar, T. Ogawa and S. Kitagawa, *Angew. Chem., Int. Ed.*, 2020, **59**, 2–15.
- 35 W. Chen, S. Horike, D. Umeyama, N. Ogiwara, T. Itakura, C. Tassel, Y. Goto, H. Kageyama and S. Kitagawa, *Angew. Chem., Int. Ed.*, 2016, **55**, 5195–5200.
- 36 Y. Ohara, A. Hinokimoto, W. Chen, T. Kitao, Y. Nishiyama, Y.-I. Hong, S. Kitagawa and S. Horike, *Chem. Commun.*, 2018, **54**, 6859–6862.
- 37 S. Horike, D. Umeyama, M. Inukai, T. Itakura and S. Kitagawa, *J. Am. Chem. Soc.*, 2012, **134**, 7612–7615.
- 38 D. Umeyama, S. Horike, M. Inukai and S. Kitagawa, *J. Am. Chem. Soc.*, 2013, **135**, 11345–11350.
- 39 S. Horike, W. Chen, T. Itakura, M. Inukai, D. Umeyama, H. Asakura and S. Kitagawa, *Chem. Commun.*, 2014, **50**, 10241–10243.
- 40 D. Umeyama, N. P. Funnell, M. J. Cliffe, J. A. Hill, A. L. Goodwin, Y. Hijikata, T. Itakura, T. Okubo, S. Horike and S. Kitagawa, *Chem. Commun.*, 2015, **51**, 12728–12731.
- 41 T. D. Bennett, J.-C. Tan, Y. Yue, E. Baxter, C. Ducati, N. J. Terrill, H. H. M. Yeung, Z. Zhou, W. Chen, S. Henke, A. K. Cheetham and G. N. Greaves, *Nat. Commun.*, 2015, **6**, 8079.
- 42 N. Agmon, *Chem. Phys. Lett.*, 1995, **244**, 456–462.
- 43 D. Umeyama, S. Horike, M. Inukai, T. Itakura and S. Kitagawa, *J. Am. Chem. Soc.*, 2012, **134**, 12780–12785.
- 44 M. Inukai, S. Horike, T. Itakura, R. Shinozaki, N. Ogiwara, D. Umeyama, S. Nagarkar, Y. Nishiyama, M. Malon, A. Hayashi, T. Ohhara, R. Kiyanaagi and S. Kitagawa, *J. Am. Chem. Soc.*, 2016, **138**, 8505–8511.
- 45 S. Hayashi and K. Hayamizu, *Bull. Chem. Soc. Jpn.*, 1989, **62**, 3061–3068.
- 46 P. Reinert, N. Z. Logar, J. Patarin and V. Kaucic, *Eur. J. Solid State Inorg. Chem.*, 1998, **35**, 373–387.
- 47 T. Akamatsu, T. Kasuga and M. Nogami, *Adv. Mater. Res.*, 2007, **15–17**, 327–332.
- 48 S. Horike, S. Shimomura and S. Kitagawa, *Nat. Chem.*, 2009, **1**, 695.
- 49 S. Henke, A. Schneemann, A. Wütscher and R. A. Fischer, *J. Am. Chem. Soc.*, 2012, **134**, 9464–9474.
- 50 J. Canivet, A. Fateeva, Y. Guo, B. Coasne and D. Farrusseng, *Chem. Soc. Rev.*, 2014, **43**, 5594–5617.
- 51 J. E. Shelby, *Introduction to glass science and technology*, Royal Society of Chemistry, Cambridge, UK, 2nd edn, 2005.
- 52 T. Ogawa, K. Takahashi, S. S. Nagarkar, K. Ohara, Y.-I. Hong, Y. Nishiyama and S. Horike, *Chem. Sci.*, 2020, **11**, 5175–5181.
- 53 J. R. M. E. Barsoukov, *Impedance Spectroscopy Theory, Experiment, and Applications*, John Wiley & Sons, NJ, USA, 2nd edn, 2005.
- 54 P. V. Wright, *MRS Bull.*, 2002, **27**, 597–602.
- 55 H. Nakamoto, A. Noda, K. Hayamizu, S. Hayashi, H.-o. Hamaguchi and M. Watanabe, *J. Phys. Chem. C*, 2007, **111**, 1541–1548.
- 56 S.-Y. Lee, T. Yasuda and M. Watanabe, *J. Power Sources*, 2010, **195**, 5909–5914.
- 57 T. Norby, *Solid State Ionics*, 1988, **28–30**, 1586–1591.
- 58 R. Gaillac, P. Pullumbi, K. A. Beyer, K. W. Chapman, D. A. Keen, T. D. Bennett and F.-X. Coudert, *Nat. Mater.*, 2017, **16**, 1149–1154.
- 59 T. L. Greaves and C. J. Drummond, *Chem. Rev.*, 2015, **115**, 11379–11448.
- 60 A. Hayashi, K. Noi, A. Sakuda and M. Tatsumisago, *Nat. Commun.*, 2012, **3**, 856.
- 61 S. G. Bratsch, *J. Phys. Chem. Ref. Data*, 1989, **18**, 1–21.
- 62 A. J. Bard and L. R. Faulkner, *Electrochemical Methods: Fundamentals and Applications*, Wiley, 2nd edn, 2000.
- 63 Y. Q. Qiao, J. P. Tu, X. L. Wang and C. D. Gu, *J. Power Sources*, 2012, **199**, 287–292.

